

**A recipe for a great meal:
A benchtop route from elemental Se to superior thermoelectric β -Ag₂Se**

Yao Abusa,^a Philip Yox,^{ab} Gayatri Viswanathan,^{ab} Jemima Opare-Addo,^{ab} Arka Sarkar,^{ab} Victoria Kyveryga,^a Emily Smith,^{ab} Oleg I. Lebedev,^c Kirill Kovnir^{*ab}

^a *Department of Chemistry, Iowa State University, Ames, Iowa 50011, USA*

^b *Ames National Laboratory, U.S. Department of Energy, Ames, Iowa 50011, USA*

^c *Laboratoire CRISMAT, ENSICAEN, CNRS UMR 6508, 14050 Caen, France*

Corresponding author : Dr. Kirill Kovnir, kovnir@iastate.edu

Abstract: The low-temperature modification of β -Ag₂Se has proven useful as a near-room temperature thermoelectric material. Over the past years, research has been devoted to interstitial, vacancy, and substitutional doping into the parent β -Ag₂Se structure, aiming at tuning the material's charge and heat transport properties to enhance thermoelectric performance. The transformation of β -Ag₂Se into α -Ag₂Se at $\sim 134^\circ\text{C}$ and the low solubility of dopants are the main obstacles for the doping approach. Herein, we report a facile, safe, scalable, and cost-effective benchtop approach to successfully produce metal-doped β -Ag₂Se. The doped materials display a remarkable enhancement of thermoelectric performance with a record-high peak zT of 1.30 at 120°C and an average zT of ~ 1.15 in the $25\text{-}120^\circ\text{C}$ range for 0.2 at.% Zn-doped Ag₂Se. The enhancement in zT is attributed to point defects created by Zn doping into Ag vacancies/interstitials, which enhanced the scattering of phonons and tuned the charge carrier properties – leading to the significant suppression of thermal conductivity. The simplicity of the synthetic method developed herein, and the high performance of the final products provides an avenue to produce high-quality Ag₂Se-based thermoelectric materials.

Keywords: benchtop synthesis; thermoelectrics; doping; polymorphism.

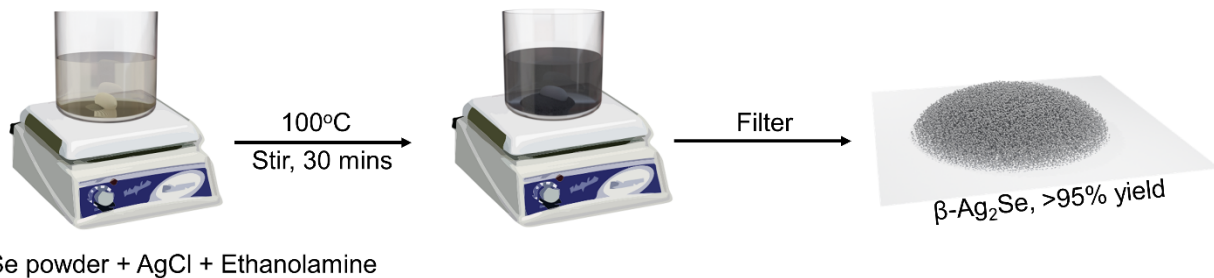
Introduction. Over-dependence on fossil fuels and the high depletion of our ecosystem has prompted intensive research in renewable energy and efficient energy utilization. As a potential strategy to optimize energy efficiency and achieve carbon neutrality, thermoelectric (TE) technology has drawn considerable attention.^{1,2} TE technology employs materials that can directly convert heat into electrical power and vice versa. TEs can harvest low-grade waste heat from the environment to be utilized for a plethora of applications. The TE energy conversion efficiency depends on a dimensionless figure-of-merit, $zT = S^2\sigma T/\kappa_{\text{tot}}$, where S , σ , T , and κ_{tot} represent the Seebeck coefficient, the electrical conductivity, the absolute temperature, and the total thermal conductivity, respectively. The latter is comprised of two parts, the electronic (κ_e) and lattice (κ_l) thermal conductivities.³⁻⁵ For a high-performance TE material, a high power factor ($S^2\sigma$) and low thermal conductivity are essential.⁶ However, these parameters are coupled and adversely related, making it challenging to optimize zT . Band structure engineering approaches through doping and alloying have been implemented to tune the carrier concentration (n) and carrier mobility (μ) of TE materials – a strategy which has been successful in optimizing the TE power factor.⁷⁻⁹ Likewise, structural engineering through the creation of atomic-level defects, nanoscale grain boundaries, and hierarchical architectures aimed at enhancing phonon scattering have also been adopted to decrease thermal conductivity.¹⁰⁻¹² As a result of these modifications, there has been tremendous success in developing advanced inorganic TE materials with high performance, particularly for moderate and high temperature operations. Unfortunately, TE materials operating at near room temperatures have seen less drastic improvement in recent years.

The emergent chalcogenide thermoelectric material, n -type β -Ag₂Se, has the potential to replace the currently utilized Bi₂Te₃-based thermoelectric for near-room temperature applications. The need for this replacement stems from the low performance of n -type Bi₂Te₃-based materials and the low abundance of tellurium (0.001 ppm in the earth's crust), limiting the potential cost effectiveness and application of such materials.¹³ As such, Ag₂Se-based materials are gaining increasing attention as near room temperature thermoelectrics (TEs) owing to their environmental friendliness, chemical stability, and high ductility.¹⁴ β -Ag₂Se is a narrow bandgap semiconductor (~0.07 eV) with an intrinsic n -type behavior due to the donor effect of Ag interstitials. The orthorhombic chiral β -Ag₂Se crystal structure is stable up to 134°C; above this temperature, it transforms to the high-temperature cubic modification, α -Ag₂Se, which is a superionic conductor with a high level of disorder in the Ag sublattice.¹⁵ Benefiting from its narrow bandgap and

complex crystal structure, β -Ag₂Se exhibits high electrical conductivity, moderate Seebeck coefficient, high Hall mobility, and intrinsically low lattice thermal conductivity resulting in an overall high thermoelectric figure-of-merit (zT).¹⁶ Despite these interesting properties, the material's sensitivity to stoichiometry and synthesis makes it challenging to tune its thermoelectric performance. There have been a decent number of synthetic approaches developed to boost the thermoelectric performance of this material. zT values ranging from 0.3 to 1.2 at room temperature have been reported for bulk samples; however, achieving consistent zT values within the working temperature has been challenging.¹⁵⁻²¹ The inconsistencies in zT both at room temperature and across measured temperatures have been attributed to the poor reproducibility of utilized synthetic methods and the coexistence of metastable phases with the different orthorhombic structure, which mainly arise due to the migration of Ag ions at various temperatures.²¹

High-temperature solid-state reactions have been successfully employed for the synthesis of β -Ag₂Se.^{3,21-23} The drawbacks of this method include: (i) an exposure of the sample to undesired high-temperatures, i.e. formation of the α -phase which converts into the β -phase upon cooling, which can result in trapped α -phase domains which may negatively impact the material's thermoelectric performance; (ii) challenges in doping/substitution of Ag in Ag₂Se with other metals, because the dopant solubility at high and room temperature may be quite different. Moreover, substituted/doped phases often have a metastable nature and decompose when heated to high temperatures – resulting in the formation of a secondary phase of the dopant metal selenide as inclusions with adverse thermoelectric performance. Solution-based methods have recently been adopted as alternatives for synthesizing single-phase β -Ag₂Se-based materials with decent thermoelectric performances.^{16,24-26} However, ubiquitous use of these methods is hindered by toxicity of the starting materials, bulky nature of the solvents/surfactants employed (which can also adversely impact the electronic transport of charge carriers), inconsistency in the product yield and quality, and difficulty in controlling the reaction rate. Samples made via these solution-based routes usually require further high temperature annealing to improve material performance. Other energy and time-consuming methods such as high-energy mechanical milling^{27,28} and pulsed hybrid reactive magnetron sputtering¹⁷ techniques were used to produce β -Ag₂Se materials. Se and Ag powder have been reported to react at room temperature to form phase-pure β -Ag₂Se by hand-mixing.¹⁵ However, the prolonged reaction time and limited potential for doping may prevent usability of this method in boosting the thermoelectric performance of β -Ag₂Se.

In β -Ag₂Se thermoelectrics, doping plays a crucial role in tuning the material's carrier concentration and mobility which effectively enhances thermoelectric performance. This approach proves useful in controlling the mobility of Ag⁺ ions which is essential to tuning the material's electronic structure through bandgap engineering. For instance, Tee et al. observed a drastic improvement in electrical and thermal conductivity by incorporating 1% Cu into the lattice of Ag₂Se.²⁵ They observed a record-high zT of 1.2 at 120°C, the largest reported for n -type Ag₂Se synthesized via wet chemistry. Similarly, Li et al. employed a solvothermal route to partially substitute Sn for Ag in Ag₂Se, achieving a zT of 0.9 at room temperature.¹⁹ However, attempts by Feng *et al.* to dope Zn into interstitial Ag sites via ball milling followed by spark plasma sintering (SPS) resulted in the formation of ZnSe nano-precipitates within the Ag₂Se matrix resulting in lower zT values.²⁴ The low solubility of Zn and other heterovalent dopants, coupled with Ag₂Se sensitivity to synthesis, restricts successful aliovalent doping with metals such as Zn. We hypothesized that aliovalent placement of the Zn in the interstitial/vacancy sites in Ag₂Se would modulate carrier concentration by eliminating Ag interstitials, as well as create defects to suppress the lattice thermal conductivity. Inspired by this hypothesis, we developed a simple, safe, cost-effective, and scalable solution route to successfully dope Zn into Ag₂Se. The resultant material displays a record-high maximum zT of 1.3 at 120°C and an average $zT = 1.15$ in the 25-120°C temperature range for 0.2 at.% Zn-Ag₂Se. The peak and average zT values reported in this work are the highest for this family of materials and comparable to state-of-the-art Bi₂Te₃-based and Mg-based alloys which require high-temperature treatment for synthesis.

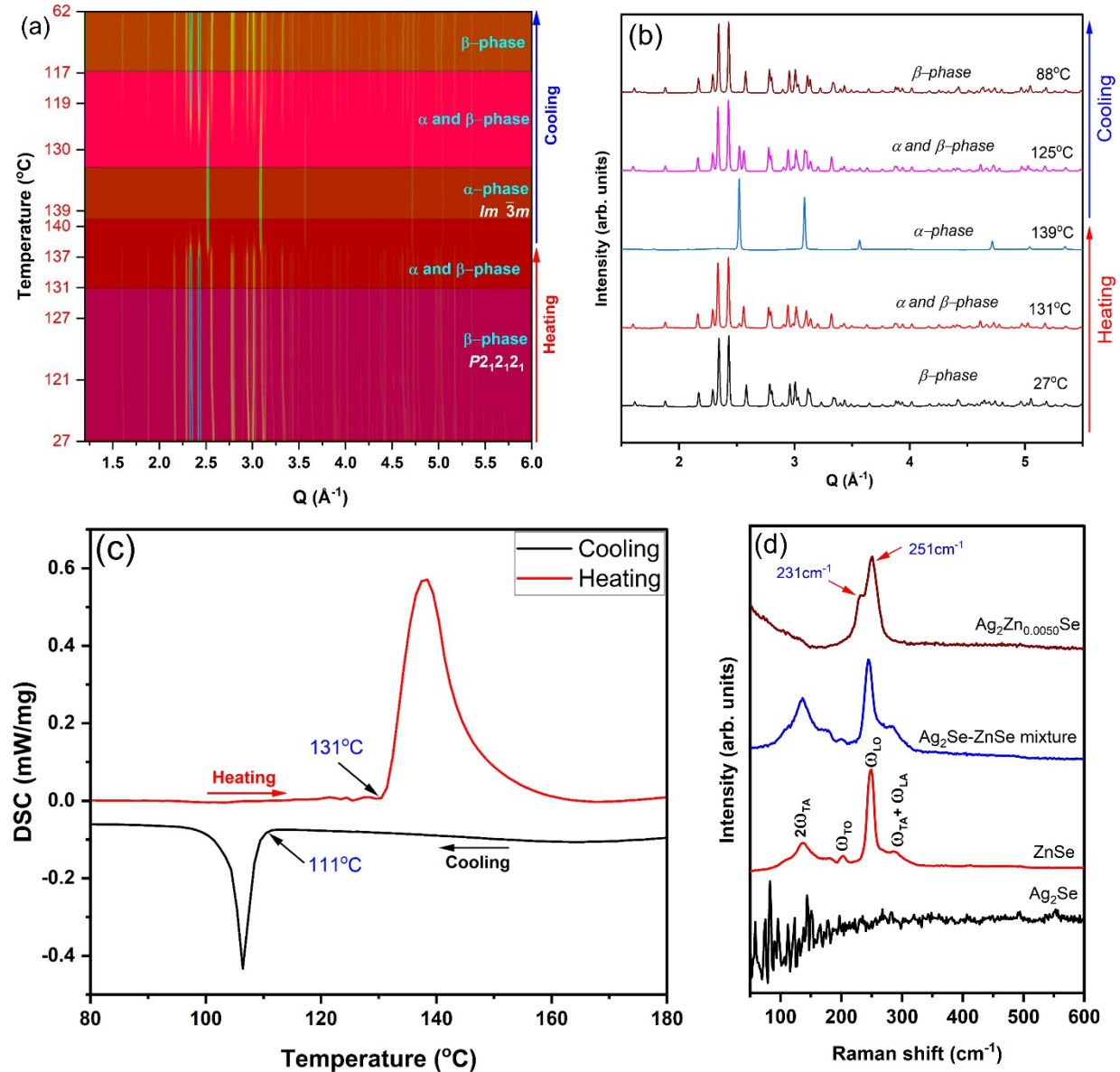


Scheme 1. Illustration of the synthetic strategy used to produce high-yield multigram batches of β -Ag₂Se.

Results and Discussion. Inspired by our work on activation of elemental Se under solvothermal conditions,²⁹ we developed a simple benchtop synthesis for silver selenide. β -Ag₂Se was synthesized using hot plate treatment of elemental selenium and solid AgCl in ethanolamine at 100°C with continuous stirring for 30 minutes (**Scheme 1**). This method produces multigram batches of phase-pure β -Ag₂Se samples with high yield (>95%). The low-temperature nature and simplicity of the developed method makes it useful for controlled doping into the Ag₂Se matrix, allowing for tuning the electronic and phonon properties. We employed this strategy to aliovalently dope Zn (<0.5 at.-%) into Ag₂Se which resulted in a remarkable enhancement of thermoelectric performance. For Zn-doped Ag₂Se samples, a solution of ZnCl₂ in ethanolamine (with different Zn concentrations) was added to beaker containing elemental Se and AgCl under the same reaction conditions described for pristine β -Ag₂Se samples (Synthesis details are provided in Supporting Information, **Figure S1**). The powder X-ray diffraction (PXRD) patterns of all samples were indexed to orthorhombic β -Ag₂Se (*P2₁2₁2₁*) with no impurity phases within the detection limit of the method.

Synchrotron temperature-dependent *in situ* PXRD was employed to analyze changes in the crystal lattices and the possible formation of secondary phases induced by Zn doping. Variation in crystal structure with temperature was also studied for possible formation of metastable phases (**Figures 1a, 1b, and S2**). As can be seen from **Figure S3**, unidentified peaks were observed around 121°C during the heating; those peaks disappeared at the phase transition to high-temperature cubic α -phase and reappeared during cooling until around 60°C before the sample fully converted back into the orthorhombic β -phase. It is noteworthy that this observation was consistent for pristine and Zn-doped samples and, as such, cannot be ascribed to the effect of Zn doping. These peaks, however, could not be assigned to any previously reported metastable Ag-Se phases,^{21,30,31} ZnSe, or elemental Ag⁰ and Se⁰ phases. Variation of the lattice parameters is negligible in the undoped and Zn-doped β -Ag₂Se samples at room temperature but varied slightly with increasing temperature due to thermal expansion. From the *in situ* diffraction experiment, Zn-doped samples undergo an $\beta \rightarrow \alpha$ phase transition from the orthorhombic to the cubic phase around 131°C while pristine Ag₂Se undergoes that transition at slightly higher temperature of 134°C (**Figure 1a, 1b and S2**). These results are consistent with other doped systems and agree well with our differential scanning calorimetry (DSC) data (**Figure 1c**). Specifically, the DSC heating curve of 0.25 at.%

Zn-doped Ag_2Se sample exhibits a relatively broad exothermic peak consistent with the gradual $\beta \rightarrow \alpha$ phase transition and a sharp endothermic peak upon cooling – indicative of a sharp $\alpha \rightarrow \beta$



phase transition.

Figure 1. (a) Contour plot and (b) selected temperature-dependent *in situ* PXRD patterns of a Zn-doped Ag_2Se sample, and (c) a DSC thermogram of the 0.25 at.% Zn-doped Ag_2Se ($\text{Ag}_2\text{Zn}_{0.0050}\text{Se}$) sample showing the transformation between cubic and orthorhombic phases. (d) Room-temperature Raman spectra of pristine Ag_2Se , ZnSe , mechanically combined mixture of $\text{Ag}_2\text{Se-ZnSe}$, and $\text{Ag}_2\text{Zn}_{0.0050}\text{Se}$.

Rietveld refinement of high-resolution room temperature synchrotron PXRD data confirmed the absence of admixture/secondary phases such as ZnSe , Zn , Se , or Ag attesting to the phase purity

of our samples (**Figures 2a, S4, S5a, and S6**). Zn-doping into β -Ag₂Se resulted in the systematic increase of the refined unit cell volume (**Figures 2b, S5b, and S7**). Since the ionic radius for Zn²⁺ (0.74 Å) is smaller than that for Ag⁺ (1.15 Å), the interstitial rather than substitutional nature of doping was hypothesized based on the overall increase of the unit cell volume. We further analyzed the pair distribution function (PDF) from total X-ray scattering experiments to characterize any amorphous phases which may not be detected by our diffraction studies. The PDF curves for both short range ($2\text{Å} \leq r \leq 5\text{Å}$) (**Figure S11**) and long range ($5\text{Å} \leq r \leq 20\text{Å}$) (**Figure S12**) were adequately fit by the orthorhombic β -Ag₂Se structural model without any amorphous impurities within the limit of the experiment, in support of the high phase purity of samples. The similarity in PDFs for both pristine and Zn-doped Ag₂Se samples is expected for such low level of doping. However, we did observe an increase in unit cell volume with Zn doping (**Figure S13**) – a result consistent with our diffraction studies.

To understand the impact of Zn dopant on the phonon interactions, we performed Raman scattering experiments (**Figure 1d**). Two peaks around 231 and 251 cm⁻¹ in the Ag₂Zn_{0.0050}Se Raman spectra have frequencies which are similar to those for the surface and longitudinal optical (ω_{LO}) phonon modes of ZnSe, respectively.³²⁻³⁵ Given that there exist two Ag sites in β -Ag₂Se structure with tetrahedral and trigonal coordination, the low frequency mode may be attributed to trigonal Zn interaction with Se atoms. To ensure that the observed modes are not from an admixture ZnSe secondary phase, we obtained a control Raman spectrum on pristine Ag₂Se, ZnSe, and mechanically combined mixture Ag₂Se-ZnSe. Pristine Ag₂Se shows no Raman vibrational modes in the studied region, consistent with previous reports.^{36,37} On the other hand, peaks corresponding to the transverse and longitudinal optical and acoustic modes of ZnSe were observed for both pristine ZnSe and the mechanically mixed Ag₂Se-ZnSe samples. Raman peaks around 200 and 250 cm⁻¹ correspond to transverse optical (ω_{TO}) and longitudinal optical (ω_{LO}) phonon modes of ZnSe, respectively. Peaks around 138 and 270 cm⁻¹ correspond to two-transverse acoustic (ω_{TA}) and double-phonon excitation ($\omega_{\text{TA}} + \omega_{\text{LA}}$) modes, respectively.^{38,39} Most of the latter modes are absent in the Raman spectrum of the Zn-doped Ag₂Se sample indicating that the observed Raman peaks cannot be ascribed to ZnSe impurities.

Energy dispersive X-ray spectroscopy (EDS) was employed to determine the atomic ratio of Ag and Se (**Table S2**). The low level of Zn doping was challenging to quantify reliably using EDS; hence, wavelength dispersive spectroscopy (WDS) was employed for Zn quantification. The slight

deficiency in Se obtained from EDS and WDS was attributed to the evaporation of Se due to the high acceleration voltage (20 kV) and small spot size employed during WDS measurements (**Table S1, Figure S8**). **Figure 2c and S9** show backscattered electron SEM images and the corresponding EDS elemental maps of Zn-doped Ag_2Se samples. A homogeneous distribution of Ag, Se, and Zn was observed, confirming the chemical uniformity of the samples. There was no observable indication of nano-precipitates of ZnSe, consistent with our high-resolution diffraction, total X-ray scattering, and Raman results, later confirmed by TEM.

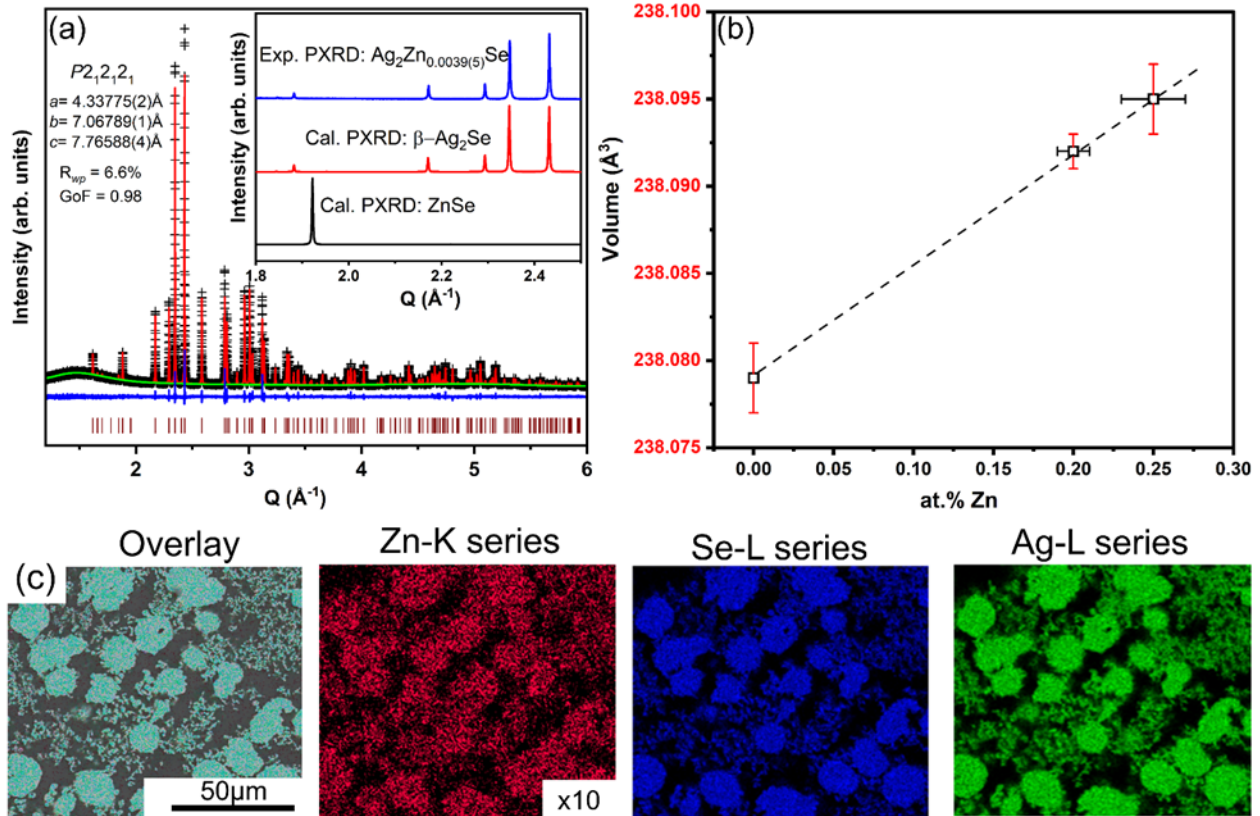


Figure 2. (a) Rietveld refinement of a room-temperature synchrotron PXRD pattern ($\lambda = 0.459723\text{\AA}$) for 0.2 at.% Zn-doped Ag_2Se . Experimental data: black crosses. Calculated pattern: red line. Difference profile: blue. Vertical ticks indicate the positions for $\beta\text{-Ag}_2\text{Se}$ peaks (space group: $P2_12_12_1$, No. 19). The inset shows a zoomed in region of the experimental diffraction pattern of Zn-doped $\beta\text{-Ag}_2\text{Se}$ along with calculated patterns for undoped Ag_2Se and ZnSe. (b) Dependence of the unit cell volume (obtained from Rietveld refinement) on the %Zn-dopant concentration as determined from WDS. (c) Backscattered SEM images and elemental mapping of 0.2 at.% Zn-doped Ag_2Se sample showing the distribution of Ag, Se, and Zn (intensity of Zn is increased by 10-fold to enhance visibility).

Doped and undoped β -Ag₂Se samples appeared to be quite sensitive to the electron beam and obtaining clear scanning-transmission electron microscopy images and diffraction patterns was challenging. Neither secondary Zn-containing phases nor Zn-rich areas were detected. HAADF-STEM EDX mapping showed a homogeneous distribution of Zn atoms across the doped sample (**Figure S22**). The precise location of Zn atoms was not possible to determine due to beam sensitivity of the samples (even using 80 kV accelerating voltage). We also cannot exclude the local displacement of the Ag atoms in the case of Zn doping, which makes a slight difference between simulated and experimental images (**Figure 3**). The observed electron diffraction patterns (**Figures S21**) and high resolution HAADF-STEM images (**Figure 3 and S23**) of 0.25 at.% Zn-doped Ag₂Se (Ag₂Zn_{0.0050}Se) sample agree well with the structural model of β -Ag₂Se. No substantial structural perturbations were detected supporting the model obtained from Rietveld and PDF refinements of synchrotron diffraction and total scattering data.

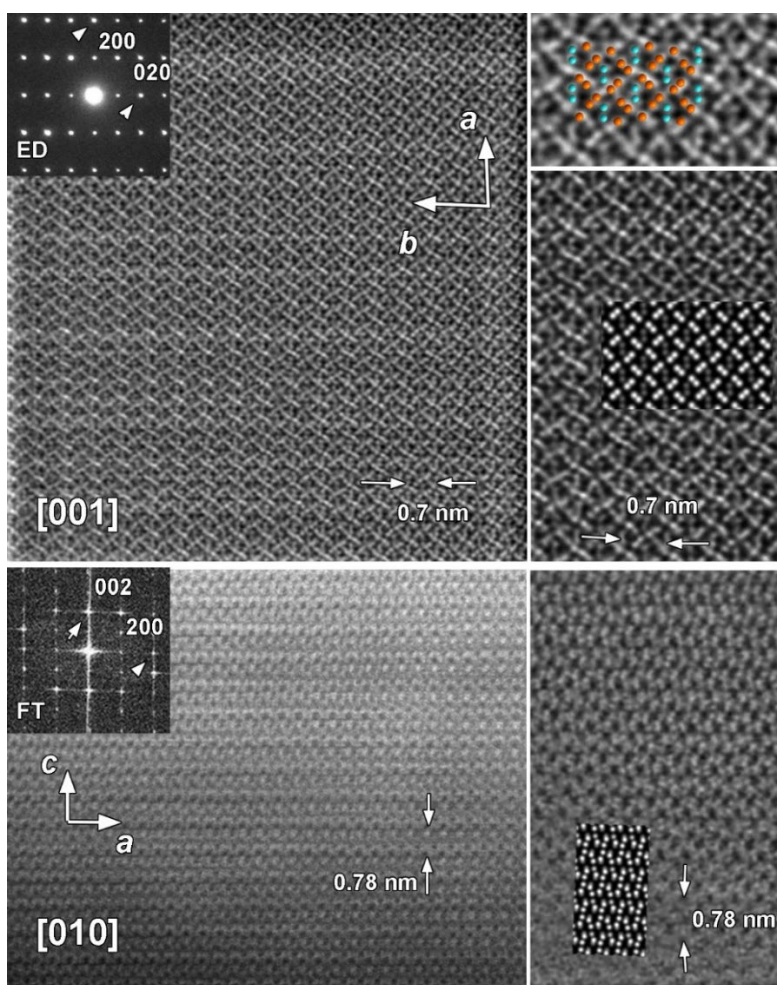


Figure 3: High resolution [001] (top) and [010] (bottom) HAADF-STEM images of the 0.25 at.% Zn-doped Ag₂Se (Ag₂Zn_{0.0050}Se) sample. The simulated images and structural models are

overlaid with the enlarged portion of each image on the right. Corresponding electron diffraction (ED) and fast Fourier transform (FFT) diffraction patterns are also shown.

The TE properties of the as-synthesized undoped and Zn-doped β -Ag₂Se samples were measured (**Figures 4 and 5**). The sharp change of all properties at $\sim 130^\circ\text{C}$ is associated with the intrusion of superionic high-temperature cubic α -Ag₂Se phase fragments in the orthorhombic lattice of β -Ag₂Se. This claim is validated by our temperature-dependent *in situ* diffraction studies, where the appearance of both phases (α and β) was observed around $\sim 130^\circ\text{C}$ (**Figure 1a**). This type of mixed lattice structure has been reported to exhibit liquid-like behavior, which promotes high carrier concentration due to the mobility of Ag ions. The coexistence of α and β phases introduces disorder in the lattice structure, which annihilates the mobility of carriers and cause a decrease in electrical conductivity, σ .^{40,41}

Electrical conductivity of the Zn-doped samples was substantially lower than that for the undoped sample (**Figure 4a**). This indicates that Zn-doping is not a simple substitution of Ag⁺ with Zn²⁺ (which is expected to increase the charge carrier concentration and electrical conductivity) but a more complex process. All samples show an increase in electrical conductivity with temperature (25-120°C) due to the intrinsic excitation of carriers (**Figure 4a**).⁴² To get a more comprehensive understanding of this phenomenon, Hall effect measurements were carried out on pristine and 0.25 at.% Zn-doped samples. The negative values obtained for Hall coefficient are indicative of *n*-type carrier transport and supported by the observed sign of Seebeck coefficient (**Figure 4b** and **S18**). Compared with the pristine undoped sample, the Zn-doped Ag₂Se sample exhibits superior Hall mobility and lower carrier concentration (**Figure 4c&d**, **Figure S16**). The reduced mobility in undoped samples may be attributed to increased carrier scattering centers introduced by Ag interstitials and vacancies. Thus, the reduction of Ag interstitials/vacancies by Zn doping diminishes carrier scattering, which results in higher carrier mobility.²¹ The significant reduction in carrier concentration in Zn-doped Ag₂Se compared with undoped sample is consistent with the observed electrical conductivity values (**Figure 4**). An estimation of the bandgap from Arrhenius plot of electrical resistivity (from 300-390 K) yielded values ranging from 0.064 to 0.095 eV for Zn-doped samples, which is smaller than the bandgap of 0.23 eV for undoped β -Ag₂Se (**Figure S10**). The latter value of bandgap is consistent with reported values for undoped β -Ag₂Se-based materials.^{15,21}

The electrical conductivity of Zn-doped samples increases slightly (<5%) with increasing Zn content. For example, at room temperature, the electrical conductivity of $\text{Ag}_2\text{Zn}_{0.0039}\text{Se}$ is 983 S/cm, while that of $\text{Ag}_2\text{Zn}_{0.0057}\text{Se}$ sample is 1033 S/cm. We hypothesize that, at low doping levels, Zn atoms first fill Ag vacancies (Ag_v) in $\beta\text{-Ag}_2\text{Se}$ before beginning to fill interstitial sites. The reduction in Ag vacancies diminishes the carrier scattering, resulting in a decrease in carrier concentration leading to lower σ (**Figure 4a**). With further increase in Zn content, the excess Zn atoms enter Ag interstitial sites (Ag_i) causing growth in carrier concentration and a drop in carrier mobility, similar to the recent observation for Cu doped SnSe.⁸ The electrical conductivities of all Zn-doped samples show weak temperature dependence compared to the pristine $\beta\text{-Ag}_2\text{Se}$, which can be attributed to the modified band gap. The large bandgap observed for undoped Ag_2Se stems from an offset between the conduction and valence band which increases carrier scattering centers, leading to poor carrier mobility.

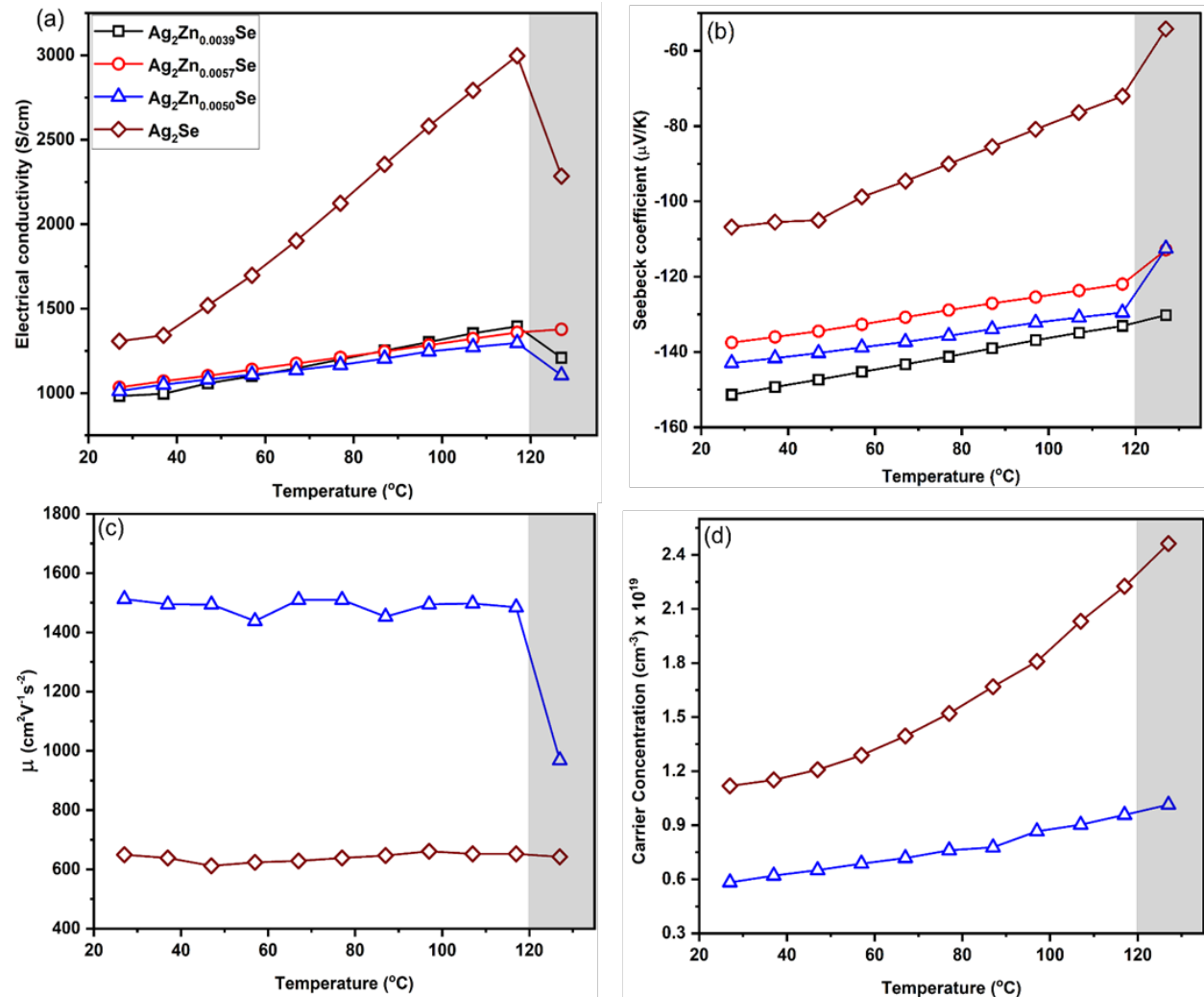


Figure 4. Temperature dependence of (a) the electrical conductivity and (b) Seebeck coefficient for β -Ag₂Se and Ag₂Zn_xSe samples ($x = 0.0039, 0.0050, \text{ and } 0.0057$ corresponding to 0.2, 0.25 and 0.3 at.% Zn doping respectively), as well as (c) Hall mobility and (d) carrier concentration of β -Ag₂Se and Ag₂Zn_{0.0050}Se. The two-phase ($\beta \rightarrow \alpha$) region is shaded in gray.

From low-temperature measurements of electrical resistivity for Ag₂Zn_{0.0050}Se (**Figure S14**), we observed that below 100 K, the concentration of charge carriers remains constant and electron scattering resulted in increased resistivity, indicating metallic behavior. As temperature increases, the electrical conductivity becomes activated, and a typical semiconducting behavior is observed. To check the reproducibility of the observed properties, we measured electrical conductivity using three different instruments: a Quantum Design Physical Property Measurement System (PPMS), Netzsch SBA 458 Nemesis, and LINSEIS LSR-3. All measurements provided reproducible results with conductivity values of 1000-1075 S/cm at room temperature (**Figure S15**). For the discussion of thermoelectric properties in this paper, we conservatively selected the Netzsch SBA 458 Nemesis data because it provided the lowest values of power factor, resulting in the lowest zT values.

Figure 4b depicts trends for the temperature dependence of Seebeck coefficient (S) for n -type β -Ag₂Se. A decrease in absolute values of S with increasing temperature is observed for all samples and consistent with previous reports for n -type semiconductors.⁴² The inverse relationship between S and n results in a decrease in the thermopower with an increase in carrier concentration, a phenomenon indicative of single-band transport.⁴ The remarkable improvement in S for Zn-doped Ag₂Se compared with the undoped sample benefited from a decrease in carrier concentration.

The temperature dependencies of thermal conductivity for all samples are presented in **Figure 5a**. All Zn-doped samples have low thermal conductivity (below 0.8 W/mK prior to the phase transition) over the measured temperature range (25-130°C). The electronic thermal conductivity ($\kappa_e = L\sigma T$, where L is the Lorenz number) was estimated from the Seebeck coefficient data (**Figure S17a**). From κ_e , the lattice thermal conductivity, κ_L , was computed ($\kappa_{\text{tot}} - \kappa_e$) (**Figure S17b**). The values of κ_L for our Zn-doped samples across the measured temperature range are ultralow and close to the glassy limit for crystalline materials. Ultralow lattice thermal conductivities were reported for materials with some degree of disorder in the crystal structures.^{21,43-45} The relatively low total thermal conductivity could be attributed to two phenomena. First, the reduced electrical conductivity, originating from the reduced carrier concentration, suppresses κ_e (**Figure S17a**).^{5,24} Furthermore, introducing Zn into Ag vacancies/interstitials may give rise to point defects or impact

the ionic migration, leading to increased phonon scattering and decreased lattice thermal conductivity (**Figure S17b**). Yet, the lattice thermal conductivity weakly depends on the Zn dopant concentration. Further studies are necessary to clarify the underlying relationships between Zn doping and lattice thermal conductivity.

The sudden rise in thermal conductivity at 130°C to ~1.6 W/mK for all samples (**Figure 5a**) results from an increase in specific heat capacity at the phase transition as discussed by *Chen et al.*^{2,44}

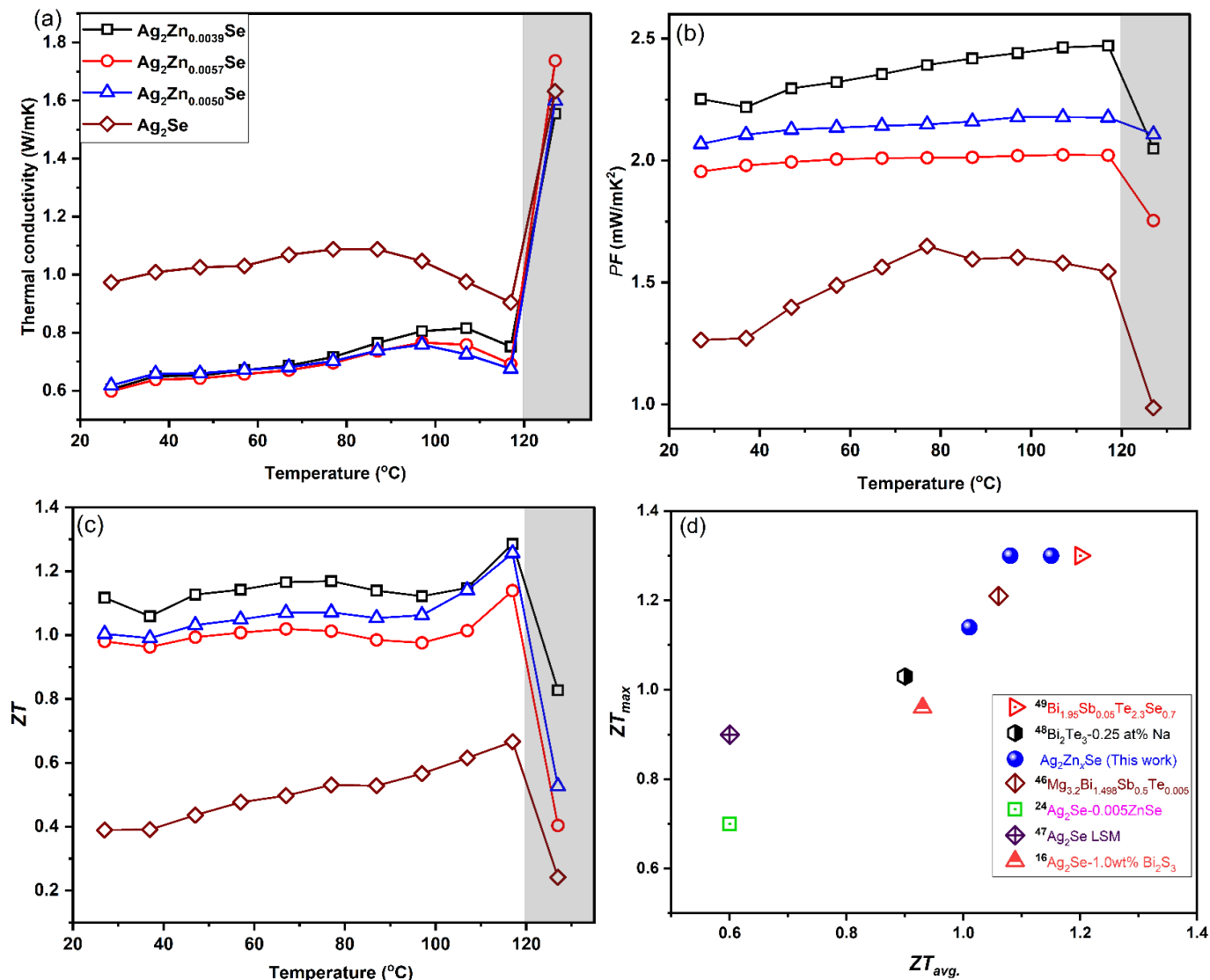


Figure 5. Temperature dependence of (a) total thermal conductivity, (b) power factor, and (c) zT for pristine β - Ag_2Se and doped $\text{Ag}_2\text{Zn}_x\text{Se}$ samples ($x = 0.0039, 0.0050,$ and 0.0057 corresponding to 0.2, 0.25 and 0.3 at.% Zn doping respectively). The two-phase ($\beta \rightarrow \alpha$) region is shaded in gray. (d) Comparison of the peak and average zT of Zn-doped β - Ag_2Se samples (25-120°C) against other state-of-the-art room-temperature thermoelectric materials.

To determine whether sintering temperature impacts the electrical and thermal transport properties of Zn-doped β -Ag₂Se samples, we synthesized an additional batch of 0.25 at.% Zn-doped Ag₂Se and consolidated it into pellets at 100 °C (SPS-100) and 200 °C (SPS-200). In the range of 25-90 °C, we observed significantly lower electrical conductivity in SPS-200 compared with SPS-100 (**Figure S19**). With sample exposure to temperatures above the $\beta \rightarrow \alpha$ phase transition during sintering, tiny inclusions of α -Ag₂Se phase in the β -Ag₂Se matrix may form and impede the concentration of carriers resulting in lower electrical conductivity. As we approach the phase transition (90-127 °C), the electrical conductivity is more similar between SPS-100 and SPS-200, although SPS-200 still lags until ~115 °C. The drop in carrier concentration slightly impacts the Seebeck coefficient and thermal conductivity between 25-90 °C, and levels up with SPS-100 at high temperatures (**Figure S19**). Thus, exposing Ag₂Se samples to temperatures above the $\beta \rightarrow \alpha$ phase transition during synthesis and/or post-synthetic treatment may be detrimental to the transport properties. This reinforces the need to carry out synthesis and material processing at temperatures below 130 °C, favoring solution-based synthetic approaches.

The temperature-dependent power factors (PF) (**Figure 5b**) for all Zn-doped samples gradually increased from room temperature to 100 °C and remained constant till 120 °C; after this temperature, PF decreases due to the onset of the $\beta \rightarrow \alpha$ phase transition. The maximum PF for Zn-doped samples is about 2-fold higher than in the undoped sample. Owing to the well-maintained high electrical transport properties (PF) and the largely suppressed thermal conductivity resulting from Zn doping, the zT values of β -Ag₂Se can be enhanced via Zn doping from 0.7 to 1.3 at 120 °C (**Figure 5c**). Besides boosting the peak value, the average zT values across the whole temperature range (25-120 °C) were also tremendously improved to 0.98-1.15 for different Zn concentrations. For traditional Bi₂Te₃-based thermoelectric materials, low performance of the n -type materials limits the energy conversion efficiency of room-temperature thermoelectric modules. We envision that the simplicity of synthesis and enhanced average zT values in n -type Zn-doped Ag₂Se materials should push forward the applications for such thermoelectric devices.

Conclusions. We have demonstrated that uniformly Zn-doped Ag₂Se samples can be facily synthesized by utilizing benchtop chemistry starting from benign reagents, elemental Se, AgCl, and ZnCl₂. Synthesis and sintering of pellets at 100 °C avoid the formation of high-temperature phases because samples are never exposed to temperatures above the $\beta \rightarrow \alpha$ phase transition. Our results show that Zn can be successfully doped on the level of up to 0.3 at.% into the β -Ag₂Se

matrix which drastically modifies transport properties of the material. Owing to the controlled level of doping and low synthetic/processing temperatures, Zn-doped samples produced in the present work demonstrated remarkable thermoelectric performance with a maximum zT of 1.3 and averaged zT of 1.15 in 25-120°C range which outperforms all reported β -Ag₂Se materials and is on par with the best n -type Bi₂Te₃-based and Mg₃Bi₂-based materials (**Figure 5d and S20**).^{24,46-49} The latter materials require high-temperatures and complex synthetic modifications, while our synthesis employs a simple and sustainable benchtop chemistry to yield efficient room temperature thermoelectric materials.

Supporting Information

The Supporting Information is available free of charge: Description of synthetic and characterization experimental procedures and additional figures and tables pertaining to powder X-ray diffraction, synchrotron total scattering, in-situ powder diffraction, crystallographic data, EDS/WDS elemental analysis, scanning and scanning-transmission electron microscopy elements maps, transport properties, electron diffraction and high resolution HAADF-STEM images and literature thermoelectric performance values for Ag₂Se.

AUTHOR INFORMATION

Corresponding Author

Dr. Kirill Kovnir, kovnir@iastate.edu

Author Contributions

The manuscript was written through contributions of all authors.

Funding Sources

This research was supported by the National Science Foundation grants DMR- 2333388 to KK. Use of the Advanced Photon Source was supported by U.S. Department of Energy, Office of Basic Energy Sciences, under Contract No. DE-AC02-06CH11357. The PPMS and LSR-3 LINSEIS instruments used for property measurements were supported by Ames National Laboratory, U.S. Department of Energy, Office of Science, Office of Basic Energy Sciences, Materials Sciences and Engineering Division. Ames National Laboratory is operated for the U.S. Department of Energy by Iowa State University under Contract No. DE-AC02-07CH11358.

Acknowledgements

The authors would like to thank Dr. W. Straszheim (MARL-ISU) for the help with SEM/EDS/WDS data collection; Prof. J.V. Zaikina (ISU) for access to the SPS; Dr. W. Xu, Dr. S. Lapidus, and Dr. O.J Borkiewicz for help with conducting *in situ* PXRD, high-resolution synchrotron PXRD, and total X-ray scattering measurements at beamlines 17-BM, 11-BM, and 11-ID-B at APS-ANL, respectively; and to A. Kovnir (Kyiv, Ukraine) for the help with TOC image.

References

- (1) Gayner, C.; Amouyal, Y. Energy Filtering of Charge Carriers: Current Trends, Challenges, and Prospects for Thermoelectric Materials. *Adv. Func. Mater.* **2020**, *30* (18), 1901789.
- (2) Mao, J.; Chen, G.; Ren, Z. Thermoelectric Cooling Materials. *Nat. Mater.* **2021**, *20* (4), 454–461.
- (3) Day, T.; Drymiotis, F.; Zhang, T.; Rhodes, D.; Shi, X.; Chen, L.; Snyder, G. J. Evaluating the Potential for High Thermoelectric Efficiency of Silver Selenide. *J. Mater. Chem. C* **2013**, *1* (45), 7568–7573.
- (4) Rawat, P. K.; Paul, B.; Banerji, P. Exploration of Zn Resonance Levels and Thermoelectric Properties in I-Doped PbTe with ZnTe Nanostructures. *ACS Appl. Mater. Interfaces* **2014**, *6* (6), 3995–4004.
- (5) Snyder, G. J.; Toberer, E. S. Complex Thermoelectric Materials. *Nature Mater* **2008**, *7* (2), 105–114.
- (6) Channegowda, M.; Mulla, R.; Nagaraj, Y.; Lokesh, S.; Nayak, S.; Mudhulu, S.; Rastogi, C. K.; Dunnill, C. W.; Rajan, H. K.; Khosla, A. Comprehensive Insights into Synthesis, Structural Features, and Thermoelectric Properties of High-Performance Inorganic Chalcogenide Nanomaterials for Conversion of Waste Heat to Electricity. *ACS Appl. Energy Mater.* **2022**, *5* (7), 7913–7943.
- (7) Heremans, J. P.; Jovovic, V.; Toberer, E. S.; Saramat, A.; Kurosaki, K.; Charoenphakdee, A.; Yamanaka, S.; Snyder, G. J. Enhancement of Thermoelectric Efficiency in PbTe by Distortion of the Electronic Density of States. *Science* **2008**, *321* (5888), 554–557.
- (8) Liu, D.; Wang, D.; Hong, T.; Wang, Z.; Wang, Y.; Qin, Y.; Su, L.; Yang, T.; Gao, X.; Ge, Z.; Qin, B.; Zhao, L.-D. Lattice Plainification Advances Highly Effective SnSe Crystalline Thermoelectrics. *Science* **2023**, *380* (6647), 841–846.
- (9) Biswas, K.; He, J.; Zhang, Q.; Wang, G.; Uher, C.; Dravid, V. P.; Kanatzidis, M. G. Strained Endotaxial Nanostructures with High Thermoelectric Figure of Merit. *Nature Chem* **2011**, *3* (2), 160–166.
- (10) Biswas, K.; He, J.; Blum, I. D.; Wu, C.-I.; Hogan, T. P.; Seidman, D. N.; Dravid, V. P.; Kanatzidis, M. G. High-Performance Bulk Thermoelectrics with All-Scale Hierarchical Architectures. *Nature* **2012**, *489* (7416), 414–418.
- (11) Pei, Y.; Zheng, L.; Li, W.; Lin, S.; Chen, Z.; Wang, Y.; Xu, X.; Yu, H.; Chen, Y.; Ge, B. Interstitial Point Defect Scattering Contributing to High Thermoelectric Performance in SnTe. *Adv. Electron. Mater.* **2016**, *2* (6), 1600019.
- (12) Pei, Y.; Shi, X.; LaLonde, A.; Wang, H.; Chen, L.; Snyder, G. J. Convergence of Electronic Bands for High Performance Bulk Thermoelectrics. *Nature* **2011**, *473* (7345), 66–69.
- (13) Han, Z.; Li, J.-W.; Jiang, F.; Xia, J.; Zhang, B.-P.; Li, J.-F.; Liu, W. Room-Temperature Thermoelectric Materials: Challenges and a New Paradigm. *J. Mater.* **2022**, *8* (2), 427–436.
- (14) Lim, K. H.; Wong, K. W.; Liu, Y.; Zhang, Y.; Cadavid, D.; Cabot, A.; Ng, K. M. Critical Role of NanoInclusions in Silver Selenide Nanocomposites as a Promising Room Temperature Thermoelectric Material. *J. Mater. Chem. C* **2019**, *7* (9), 2646–2652.
- (15) Yang, D.; Su, X.; Meng, F.; Wang, S.; Yan, Y.; Yang, J.; He, J.; Zhang, Q.; Uher, C.; Kanatzidis, M. G.; Tang, X. Facile Room Temperature Solventless Synthesis of High Thermoelectric Performance Ag₂Se via a Dissociative Adsorption Reaction. *J. Mater. Chem. A* **2017**, *5* (44), 23243–23251.
- (16) Nan, B.; Li, M.; Zhang, Y.; Xiao, K.; Lim, K. H.; Chang, C.; Han, X.; Zuo, Y.; Li, J.; Arbiol, J.; Llorca, J.; Ibáñez, M.; Cabot, A. Engineering of Thermoelectric Composites

- Based on Silver Selenide in Aqueous Solution and Ambient Temperature. *ACS Appl. Electron. Mater.* **2023**, *in press*, <https://doi.org/10.1021/acsaelm.3c00055>.
- (17) Perez-Taborda, J. A.; Caballero-Calero, O.; Vera-Londono, L.; Briones, F.; Martin-Gonzalez, M. High Thermoelectric zT in n-Type Silver Selenide Films at Room Temperature. *Adv. Energy Mater.* **2018**, *8* (8), 1702024.
 - (18) Aliev, F. F.; Jafarov, M. B.; Eminova, V. I. Thermoelectric Figure of Merit of Ag_2Se with Ag and Se Excess. *Semiconductors* **2009**, *43* (8), 977–979.
 - (19) Li, D.; Zhang, J. H.; Li, J. M.; Zhang, J.; Qin, X. Y. High Thermoelectric Performance for an Ag_2Se -Based Material Prepared by a Wet Chemical Method. *Mater. Chem. Front.* **2020**, *4* (3), 875–880.
 - (20) Mi, W.; Qiu, P.; Zhang, T.; Lv, Y.; Shi, X.; Chen, L. Thermoelectric Transport of Se-Rich Ag_2Se in Normal Phases and Phase Transitions. *Appl. Phys. Lett.* **2014**, *104* (13), 133903.
 - (21) Jood, P.; Chetty, R.; Ohta, M. Structural Stability Enables High Thermoelectric Performance in Room Temperature Ag_2Se . *J. Mater. Chem. A* **2020**, *8* (26), 13024–13037.
 - (22) Ferhat, M.; Nagao, J. Thermoelectric and Transport Properties of β - Ag_2Se Compounds. *J. Appl. Phys.* **2000**, *88* (2), 813–816.
 - (23) Conn, J. B.; Taylor, R. C. Thermoelectric and Crystallographic Properties of Ag_2Se . *J. Electrochem. Soc.* **1960**, *107* (12), 977.
 - (24) Feng, B.; Cheng, Y.; Liu, C.; Gao, J.; Wu, G.; Bai, X.; Si, R.; Li, W.; Guo, Y.; Miao, L. Ag Interstitial Inhibition and Phonon Scattering at the ZnSe Nano-Precipitates to Enhance the Thermoelectric Performance of Ag_2Se . *ACS Appl. Energy Mater.* **2023**, *6*, 2804–2811.
 - (25) Tee, S. Y.; Tan, X. Y.; Wang, X.; Lee, C. J. J.; Win, K. Y.; Ni, X. P.; Teo, S. L.; Seng, D. H. L.; Tanaka, Y.; Han, M.-Y. Aqueous Synthesis, Doping, and Processing of n-Type Ag_2Se for High Thermoelectric Performance at Near-Room-Temperature. *Inorg. Chem.* **2022**, *61* (17), 6451–6458.
 - (26) Tee, S. Y.; Ponsford, D.; Tan, X. Y.; Wang, X.; Lay, C. L.; Lee, C. J. J.; Ni, X. P.; Seng, D. H. L.; Thitsartarn, W.; Guan, G.; Han, M.-Y. Compositionally Tuned Hybridization of n-Type Ag^0 : Ag_2Se under Ambient Conditions towards Excellent Thermoelectric Properties at Room Temperature. *Mater. Chem. Front.* **2023**, *7* (12), 2411–2418.
 - (27) Chen, J.; Sun, Q.; Bao, D.; Liu, T.; Liu, W.-D.; Liu, C.; Tang, J.; Zhou, D.; Yang, L.; Chen, Z.-G. Hierarchical Structures Advance Thermoelectric Properties of Porous n-Type β - Ag_2Se . *ACS Appl. Mater. Interfaces* **2020**, *12* (46), 51523–51529.
 - (28) Lee, C.; Park, Y.-H.; Hashimoto, H. Effect of Nonstoichiometry on the Thermoelectric Properties of a Ag_2Se Alloy Prepared by a Mechanical Alloying Process. *J. Appl. Phys.* **2007**, *101* (2), 024920.
 - (29) Abusa, Y.; Yox, P.; Cady, S. D.; Viswanathan, G.; Opare-Addo, J.; Smith, E. A.; Mudryk, Y.; Lebedev, O. I.; Perras, F. A.; Kovnir, K. Make Selenium Reactive Again: Activating Elemental Selenium for Synthesis of Metal Selenides Ranging from Nanocrystals to Large Single Crystals. *J. Am. Chem. Soc.* **2023**, *145*(41), 22762–22775.
 - (30) Tappan, B. A.; Zhu, B.; Cottingham, P.; Mecklenburg, M.; Scanlon, D. O.; Brutchey, R. L. Crystal Structure of Colloidally Prepared Metastable Ag_2Se Nanocrystals. *Nano Lett.* **2021**, *21* (13), 5881–5887.
 - (31) Sahu, A.; Braga, D.; Waser, O.; Kang, M. S.; Deng, D.; Norris, D. J. Solid-Phase Flexibility in Ag_2Se Semiconductor Nanocrystals. *Nano Lett.* **2014**, *14* (1), 115–121.
 - (32) Li, H.; Wang, B.; Li, L. Study on Raman Spectra of Zinc Selenide Nanopowders Synthesized by Hydrothermal Method. *J. Alloys Compd.* **2010**, *506* (1), 327–330.

- (33) Teredesai, P. V.; Deepak, F. L.; Govindaraj, A.; Sood, A. K.; Rao, C. N. R. A Raman Study of CdSe and ZnSe Nanostructures. *J. Nanosci. Nanotechnol.* **2002**, *2* (5), 495–498.
- (34) Shan, C. X.; Liu, Z.; Zhang, X. T.; Wong, C. C.; Hark, S. K. Wurtzite ZnSe Nanowires: Growth, Photoluminescence, and Single-Wire Raman Properties. *Nanotechnol.* **2006**, *17* (22), 5561.
- (35) Xu, J.; Lu, A.; Wang, C.; Zou, R.; Liu, X.; Wu, X.; Wang, Y.; Li, S.; Sun, L.; Chen, X.; Oh, H.; Baek, H.; Yi, G.-C.; Chu, J. ZnSe-Based Longitudinal Twinning Nanowires. *Adv. Eng. Mater.* **2014**, *16* (4), 459–465.
- (36) Naumov, P.; Barkalov, O.; Mirhosseini, H.; Felser, C.; Medvedev, S. A. Atomic and Electronic Structures Evolution of the Narrow Band Gap Semiconductor Ag₂Se under High Pressure. *J. Phys.: Condens. Matter* **2016**, *28* (38), 385801.
- (37) Ishii, M.; Wada, H. Raman Spectroscopic Studies of Silver-Tantalum Sulfide, Silver-Niobium Sulfide and Silver-Tantalum Selenide with Argyrodite Structures. *Mater. Res. Bull.* **1993**, *28* (12), 1269–1276.
- (38) Liu, M.; Duan, P.; Shafi, M.; Liu, W.; Zhang, W.; Zhang, C.; Hu, X.; Gao, J.; Zhang, C. Surface-Enhanced Raman Spectroscopic Activity Study on Topological ZnSe Nanostructures. *Front. Phys.* **2022**, *10*, 1057992.
- (39) Chai, Y.; Yu, X.; Cheng, H.; Chang, Z.; Tetard, L.; Bass, M.; Soileau, M. J. Surface Structure Evolution and Raman Response for Multipulse, Few-Cycle, Laser Damaged ZnSe. *Opt. Express, OE* **2021**, *29* (10), 15023–15030.
- (40) Jindal, S.; Singh, S.; Saini, G. S. S.; Tripathi, S. K. Low Temperature Thermoelectric Power Factors of Thermally Evaporated Ag₂Se Thin Films. *AIP Conf. Proc.* **2020**, *2220* (1), 090008.
- (41) Ahmad, S.; Sarkar, P.; Bhatt, P.; Bhattacharya, S.; Navaneethan, M.; Basu, R.; Bhatt, R.; Bohra, A.; Debnath, A. K.; Muthe, K. P.; Vitta, S.; Singh, A. Improved Thermoelectric Performance of Ag_{2-x}Al_xSe through Formation of AgAl Phase. *Appl. Phys. Lett.* **2022**, *121* (17), 173905.
- (42) Cao, Y.; Bai, H.; Li, Z.; Zhang, Z.; Tang, Y.; Su, X.; Wu, J.; Tang, X. Zn-Induced Defect Complexity for the High Thermoelectric Performance of n-Type PbTe Compounds. *ACS Appl. Mater. Interfaces* **2021**, *13* (36), 43134–43143.
- (43) Acharyya, P.; Ghosh, T.; Pal, K.; Rana, K. S.; Dutta, M.; Swain, D.; Etter, M.; Soni, A.; Waghmare, U. V.; Biswas, K. Glassy Thermal Conductivity in Cs₃Bi₂I₆Cl₃ Single Crystal. *Nat Commun.* **2022**, *13* (1), 5053.
- (44) Cahill, D. G.; Watson, S. K.; Pohl, R. O. Lower Limit to the Thermal Conductivity of Disordered Crystals. *Phys. Rev. B* **1992**, *46* (10), 6131–6140.
- (45) Agne, M. T.; Hanus, R.; Snyder, G. J. Minimum Thermal Conductivity in the Context of Diffusion-Mediated Thermal Transport. *Energy Environ. Sci.* **2018**, *11* (3), 609–616.
- (46) Mao, J.; Zhu, H.; Ding, Z.; Liu, Z.; Gamage, G. A.; Chen, G.; Ren, Z. High Thermoelectric Cooling Performance of n-Type Mg₃Bi₂-Based Materials. *Science* **2019**, *365* (6452), 495–498.
- (47) Li, D.; Zhang, B. L.; Ming, H. W.; Wang, L.; Zu, Y.; Qin, X. Y. Liquid-Phase Manipulation Securing Enhanced Thermoelectric Performance of Ag₂Se. *ACS Appl. Mater. Interfaces* **2021**, *13* (29), 34543–34549.
- (48) Lou, L.-Y.; Yang, J.; Zhu, Y.-K.; Liang, H.; Zhang, Y.-X.; Feng, J.; He, J.; Ge, Z.-H.; Zhao, L.-D. Tunable Electrical Conductivity and Simultaneously Enhanced Thermoelectric and Mechanical Properties in n-Type Bi₂Te₃. *Adv. Sci.* **2022**, *9* (27), 2203250.

- (49) Hu, L.; Zhang, Y.; Wu, H.; Liu, Y.; Li, J.; He, J.; Ao, W.; Liu, F.; Pennycook, S. J.; Zeng, X. Synergistic Compositional–Mechanical–Thermal Effects Leading to a Record High zT in n-Type V_2VI_3 Alloys Through Progressive Hot Deformation. *Adv. Func. Mater.* **2018**, *28* (35), 1803617.

TOC

